# A LSTM-based Neural Strategy for Diagnosis of Stator Inter-turn Faults with Low Severity Level for Induction Motors

Krish Kumar Raj
*School of Information Technology, Engineering, Mathematics and Physics*
*The University of the South Pacific*
Suva, Fiji
s11160036@student.usp.ac.fj

Sukhde Joshi
*School of Information Technology, Engineering, Mathematics and Physics*
*The University of the South Pacific*
Suva, Fiji
s11158046@student.usp.ac.fj

Rahul Kumar
*School of Information Technology, Engineering, Mathematics and Physics*
*The University of the South Pacific*
Suva, Fiji
rahul.kumar@usp.ac.fj

*Abstract* — **This paper outlines a neural-based strategy to diagnose stator-inter-turn faults (STIFs) at low severities. The proposed strategy involves the study of a state-space model for healthy and faulty SITF configuration of squirrel cage induction machine (IM). Following the acquisition of healthy and faulty 3-phase currents from the state-space models, exploratory analysis of data are conducted using principal component analysis (PCA) and independent component analysis (ICA). Thereafter, various neural and non-neural-based classifiers are trained respecting appropriate data divisions. After considering factors like the least number of trainable parameters, confidence level of the outputs and highest classification metrics, the best classification model belonged to the family of LSTM neural networks.**

*Keywords—Induction motor, Stator Inter-turn Fault, Principal Component Analysis, Machine Learning, Neural Network, State Space*

## I. INTRODUCTION

Through the years, industrial automation has been enormously progressing; this involves research in devising new Condition Monitoring (CM) schemes for IMs. These motors generally are robust and reliable machines. However, scenarios such as prolonged activity times and harsh operating conditions, among other factors [1], [2], lead to electrical and mechanical faults in the IMs. According to recent literature [1], 37% of faults in IM are stator related, where stator inter-turn short circuit faults are the most common failure events. This fault occurs in a similar case of a short circuit between two turns in the same phase winding. The shorting typically occurs whenever the winding insulations gets removed due to aging. STIFs at incipient stages are very hard to detect, and if left unnoticed with normal operation, faults such as; phase-to-phase, and phase-to-ground evolve quickly [3].

Identifying SITFs at an early stage has been a challenge and a motivational factor for individuals in the respected research field to find various methodologies to detect them. An application of both motor current signature analysis (MCSA) and motor vibration analysis (MVA) to diagnose SITFs is seen in [4], and the trained system recognizes both single and multiple faults (electrical and mechanical) simultaneously. This study tests and finds Matching Pursuit (MP) and Discrete Wavelet Transform (DWT) appropriate feature extraction methods. Moreover, fine Gaussian Support Vector Machines (SVM), fine K-Nearest Neighbors (KNN), weighted KNNs, bagged trees, and subspace KNN [4], are the few classification algorithms selected from the MATLAB Classification learner toolbox that show 100% classification accuracy in practice. However, these methods fail to output the class membership probability upon subjecting the classifier to the test sets.

Shao et al. in [5] discovered using multi-signal analysis that the merged architectures perform better than multi-channel architectures. The study used a Deep Learning (DL) model, which automated feature extraction based on motor current and vibrational data. Moreover, the analysis was done in the time-frequency domain (TFD), and the literature demonstrated the capabilities of convolutional neural network (CNN) in learning features from the image maps for each of the two input signals. Upon comparing the model with other traditional classifiers, TFD + Deep CNN (DCNN) output the best prediction accuracy of 99.87%.

Machine Learning (ML) techniques have many profound applications; however, they do not perform as expected when applied in the real world. Xiao et al. [6] states that real-world working conditions differ drastically and do not have labeled outputs – which is not the case in experimental laboratory data. With this argument, the authors utilize transfer learning methods to train a CNN which performs feature identification on the target domain (which consists of unlabeled data under varying working conditions) using a source domain (labeled data under non-varying working conditions) as reference. Maximum Mean Discrepancy (MMD) [7] is used as a regularization term to minimize feature mismatch between the two domains. The learned features are then attached to the fully connected layer, which performs the final fault classification.

One of ML's major drawback that is rarely discussed is how dependent the strategy is on the training dataset. Implementing a specifically trained algorithm to an alternate IM with different characteristics shows a reduction in accuracy for fault classification. Furthermore, a comprehensive fault diagnosis (FD) method for classification, employing a multiresolution approach built on wavelet functions, is emphasized in the works of [8]. The technique incorporates multivariate quality control charts that use statistical procedures to detect multivariate outliers. The significant advantage of this method is that it can be implemented onto any industrial motor regardless of its brand or the type of feeding system it operates on.

This paper focuses on one of IM's major faults: stator-inter-turn-fault, also known as stator short-circuit fault. This fault at the incipient stage is critical and tends to evolve quickly over time that may lead to permanent damage to the stator. Thus, early diagnosis is necessary to prevent the fault

from further developing in the motor. The proposed scheme (Fig. 1) presents a data-driven approach where a state-space model of healthy and faulty 2.2kW IM is developed. With respect to the faulted IM, the stator inter-turn faults are considered from [9]. It should be note that only low SITF severities (0.3%, 0.7%, 1.05%, 2.1%) have been considered for analysis. Along with that, PCA and ICA techniques are only used for exploratory analysis of the data. Thereafter, division of data with respect to various ratios is done to train, validate and test neural and non-neural based classifiers.

This paper is organized as follows: Section II discusses the proposed strategy while Section III shows the modelling of healthy and faulty (SITF) IM and, details on acquisition of the data. Section IV gives an insight to the data geometry using exploratory data analysis tools to choose a suitable architectures for classification. Section V presents all the results and discussions for the neural and non-neural based classifiers followed by Section VI that concludes this study and gives overview of future works.

## II. STATOR INTER-TURN FAULTS (SITFs)

The proposed SITF diagnosis scheme is inspired by recent works of literature published in [10], [11]. Fig. 1 illustrates the proposed scheme that outlines the following: fault generation with different loadings induced on IM, current signature extraction, preprocessing, data division (training, validation, and test sets), neural network (NN) and non-NN model development, training of the developed model, model prediction accuracy analysis and model comparison study.
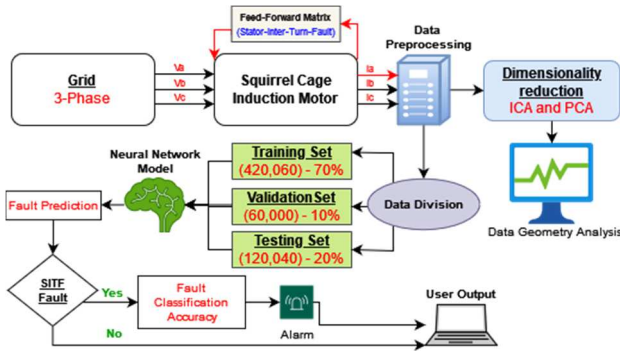


Fig. 1. Proposed scheme of IM with SITF and PCA

For simulation, the SITF has been modelled as an external stimulus to a grid controlled 3-phase healthy IM (four pole 2kW motor), which generates an additional current in the faulty phase. Knowledge of machine parameters and state space (SS) equations is essential in this process to successfully emulate the STIF in MATLAB Simulink. The resultant faulty current signatures are a summation of SITF-generated and healthy 3-phase currents. In addition, the works of [9] have inspired the SS equations.

## III. IM MODELING

### A. Healthy State Space Representation for IM

This section guides the implementation of an IM model using SS equations. The mechanical reference frame representation of IM, presenting the state vector, is shown below;

$$\dot{x} = Ax(t) + Bu(t) \tag{1}$$

$$\frac{d}{dt}\begin{bmatrix} i_s \\ \psi'_r \end{bmatrix} = \begin{bmatrix} A_{11} & A_{12} \\ A_{21} & A_{22} \end{bmatrix}\begin{bmatrix} i_s \\ \psi'_r \end{bmatrix} + \begin{bmatrix} B_1 \\ 0 \end{bmatrix} U_s \tag{2}$$

$$J\frac{dw_{rm}}{dt} + Bw_{rm} = T_{el} - T_L \tag{3}$$

$$i_s = Cx \tag{4}$$

where:

$$B = \frac{1}{(\sigma L_s)I} = bI \ , C = [I \quad 0], I = \begin{bmatrix} 1 & 0 \\ 0 & 1 \end{bmatrix} \text{and, } J = \begin{bmatrix} 0 & -1 \\ 1 & 0 \end{bmatrix}$$

This IM model operates using the Park's transformed voltages $U_{sd}$ and $U_{sq}$. The controllable states are $i_s$ stator current and $\psi'_r$ rotor flux. The flux density on the rotor surface is denoted by $B$.

The identifier matrix is represented by variable $I$ and $J$, where $I$ is the inertia coefficient matrix for this IM model. The Inertia state matrix breakdown (A) is given by:

$$A_{11} = -\left\{\frac{R_s}{\sigma L_s} + \frac{1-\sigma}{\sigma T_r}\right\}I = a_{11}I \tag{5}$$

$$A_{12} = \frac{L_m}{\sigma L_s L_r\left\{\left(\frac{1}{T_r}\right)I - w_r J\right\}} = a_{12}\left\{\left(\frac{1}{T_r}\right)I - w_r J\right\} \tag{6}$$

$$A_{22} = -\left(\frac{1}{T_r}\right)I - w_r J = a_{22}\left\{\left(\frac{1}{T_r}\right)I - w_r J\right\} \tag{7}$$

$$A_{21} = \left\{\frac{L_m}{T_r}\right\}I = a_{21}I \tag{8}$$

The $dq$ axis reference representation matrix is formulated using equation (1) and the breakdown matrices (*A, B, C, D*). The final matrix representation can be visualized in the works of [9], along with the IM model's mechanical speed equations.

### B. Stator Inter-turn Fault State Space Representation for IM

For the faulty portion of the modeling, only SITFs with very low severity is applied to the IM. This fault is best described as the shorting between turns of the stator windings producing additional current in the phases of the fault. This additional current is theoretically categorized as disturbance and represented as a direct transition or a feed-forward matrix in the SS equation. Additional parameters such as; short-circuit flux, $\phi_{cc}$, short-circuit winding, $B_{cc}$, short-circuit current, $i_{cc}$, are also considered. An elaborate detail can be found in the works of [12], [13].

The following equation describes the new output due to the presence of these disturbances.

$$y(t) = Cx(t) + Du(t) \tag{9}$$

where:
- $u(t)$, $y(t)$, and $x(t)$ are respectively the system input, output, and state variables.
- $C$ is the output matrix of constants

$$C = \begin{bmatrix} 1 & 0 & 0 & 0 \\ 0 & 1 & 0 & 0 \end{bmatrix} \tag{10}$$

- $D$ is the direct transition matrix

$$D = \sum_{k=1}^{3} \frac{2n_{cck}}{3R_s} P(-\theta)Q(\theta_{cck})P(\theta) \tag{11}$$

- $P(\theta)$, $P(-\theta)$, and $Q(\theta cck)$ are respectively the Park, inverse Park, and rotational matrices respectively (12-13).

$$P(\theta) = \begin{bmatrix} \cos(\theta) & -\sin(\theta) \\ \sin(\theta) & \cos(\theta) \end{bmatrix} \tag{12}$$

$$Q(\theta_{cck}) = \begin{bmatrix} \cos(\theta_{cck})^2 & \cos(\theta_{cck})\sin(\theta_{cck}) \\ \cos(\theta_{cck})\sin(\theta_{cck}) & \sin(\theta_{cck})^2 \end{bmatrix} \tag{13}$$

$$\text{STIF \%} = \frac{n_{cck}}{n_s * 3_{phase}} * 100 \tag{14}$$

The following variables identify the direct transition (or feedforward) matrix (11):

- $n_{cck}$ quantifies the SITF and is the ratio of the number of inter-turn short circuit winding in phase $k$ and the number of turns in a healthy phase.

- $\theta_{cck}$ is 0 for phase $A$, $2\pi/3$ for phase $B$, and $4\pi/3$ for phase $C$

- $R_s$ is the stator resistance that is obtained from the DC test results

- $k$ is the phase containing the short-circuit, and the only accepted values are 1, 2, and 3 (denoting each phase)

- $n_s$ is the number of turns in a phase

### C. Data Acquisition

A complete dataset was obtained from numerous simulation trials, with various loading levels and fault severity varying each time. In total, twenty trials were performed to account for five different machine states at four loading levels, which were at; no load (0 Nm), 50% load (3.5 Nm), 75% load (5.25 Nm), and full load (7 Nm). These trials were performed respecting the machine's maximum torque rating of 7 Nm. Moreover, at a sampling rate of 5 kHz, 30000 individual samples were obtained for the 3-phases. A total of five class datasets have been sorted, class 1 (Healthy), and class 2-5 (SITFs at ranging severities). A description of the above can be seen in Table I, where the fault severity (%) is computed using equation (14).

TABLE I. CLASS LABEL DETAILS

| Fault Class | Fault severity | Inter-turns shorted |
|---|---|---|
| 1 | Healthy | 0 |
| 2 | 0.3% | 1 |
| 3 | 0.7% | 2 |
| 4 | 1.05% | 3 |
| 5 | 2.1% | 6 |

In the data division phase, the global dataset totaled 600,100 samples. It contained three features (normalized principal components) and one hot encoded class label. The training, validation, and test sets have been divided accordingly as such;

- Training (420,060) – 70%
- Testing (120,040) – 20%
- Validation (60,000) –10%

## IV. DATA GEOMETRY AND VISUALIZATION

The 3-phase currents are visualized to understand the electrical impact of the STIF fault. It is hypothesized that the severity of the fault is directly proportional to the amplitude of the 3-phase currents. Moreover, the faulty phase should receive a higher current compared to its other two counterparts. This is because the SITF phenomenon lowers the resistance in the affected phase, causing unbalance. Hence, increasing the value of the current. Furthermore, to support the above statements, Fig. 3 shows the current amplitudes increment as the IM model deviates from healthy to faulty state.
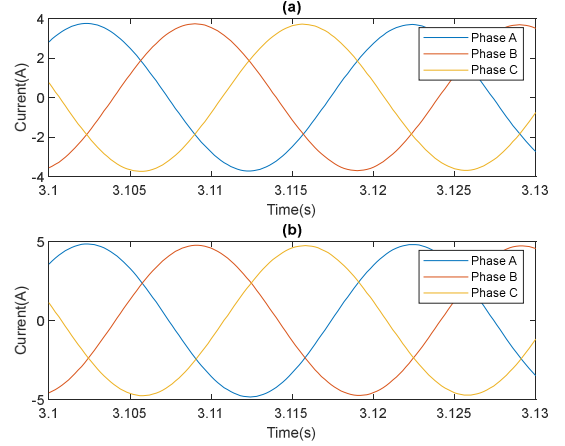


Fig. 2. (a) Healthy IM 3-Phase Currents – Full Load, (b) 0.7% fault severity IM 3-Phase Currents – Full Load

Figs. 2a-b illustrates the 3-phase currents of the healthy and faulty IM model with 0.7% severity (2-shorted turns), respectively. Both the plots are under 100% loading condition (7 Nm) considering the derived to IM model in the preceding section. For the healthy 3-phase current plot, peak values were measured to be 3.69 A, portraying normal operation of the IM. The SITFs were emulated for the faulty model in phase A of the IM. The reason why the faulty phase receives a higher current than its other two counterparts is because the STIF phenomenon lowers resistance in the affected phase, causing and unbalance among the phases, thus, the presence of spikes in the phase currents.
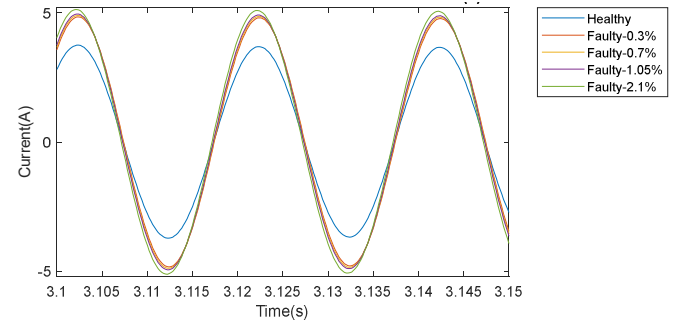


Fig. 3. Healthy and Faulty Induction Motor Phase A plots

The Pareto charts give an indication on the intrinsic dimensionality of the data. In case of PCA, they give information on the variability data in the descending order of principal components (PCs). For the generated dataset, Fig. 4a illustrates that first two components are sufficient enough to explain more than 95% of the variability in the dataset.
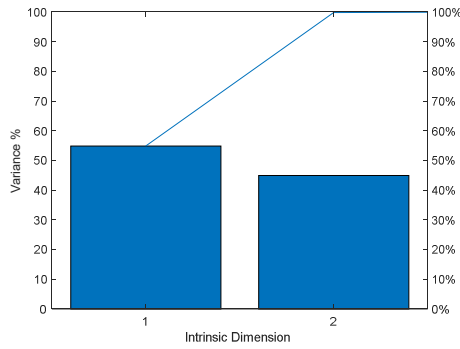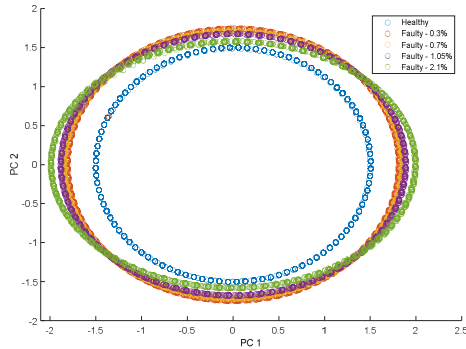
Fig. 4a. Pareto Chart
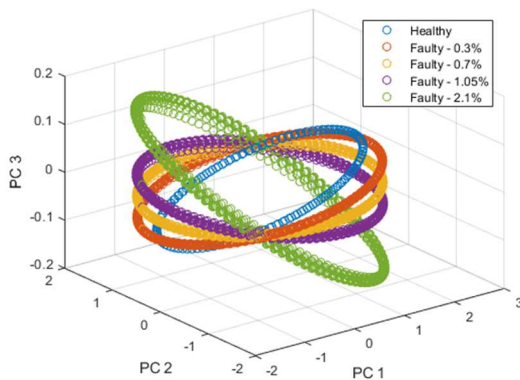


Fig. 4b. 2D PCA plot of IM at no load



Fig. 4c. 3D PCA plot of IM at no load

In this section, PCA and ICA dimensionality reduction (DR) techniques have been used to **only** study the geometry of the data, where no form of transforming or reducing the dimensionality of data is done. Through visual analysis, Fig. 4b-c shows the PCA five class clusters positioned in the 2D plane (2 PCs) and 3D plane (3 PCs), respectively. In the 2D plot (Fig. 4b), the healthy class cluster is seen to be well separated from the four faulty classes. The healthy class points are represented in an approximately circular shape. In contrast, for the faulty class clusters, the points projected on the plane seem more elliptical in nature as the fault severity increases. In the scenario of increasing loading levels (50 % - 3.5 Nm and 100 % - 7 Nm) in the 2D PCA plot, the healthy class projection remains unmoved, whereas the four fault class clusters further separate from the healthy class clusters [9]. The reasoning is the different level of fault classes with the incrementing loading levels causes abrupt changes in the current signals, which make the fault points stand out from the healthy data points. In addition, during incremented loading levels, the fault class clusters become larger in

surface area and caters more overlapping on each other, making it tough to distinguish between the fault class clusters.

As for the 3D plot (3 PCs) Fig. 4c, each of the five class clusters can be easily distinguished as the separation is well presented. The healthy class cluster (blue data points) in plot appears elliptical and roughly inclined at a 30° angle concerning PC 1 and PC 2 planes. Hence, using the healthy class cluster as a reference, the four fault clusters, which are also elliptical, tend to rotate in a clockwise motion away from the healthy class plot. It can be observed the highest fault class (2.1% - green data points) has moved the furthest from the healthy clusters. In addition, in the 3D PCA plot with (50 % and 100 % loading levels), the plots are presented in [9]. An observation made during the case of incrementing load in IM, each class cluster's plot surface area tends to widen with respect to the loading level. Still, for the same classes, the clusters' positioning is unaffected, which is similar to Fig. 4c.
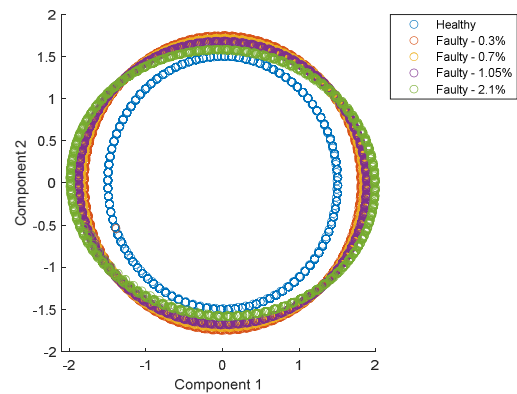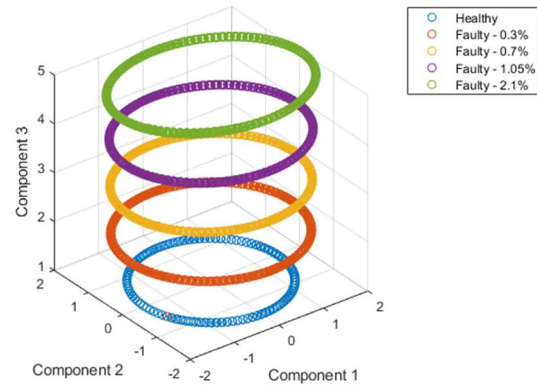


Fig. 4d. 2D ICA plot of IM with no load



Fig. 4e. 3D ICA plot of IM with no load

Another linear, fast and reliable DR technique is the ICA, which is also a good candidate for visualizing data. Figs. 4d-e illustrate the five class clusters positioned in the 2D plane and 3D plane, respectively using ICA. For Fig. 4d the class clusters appear to be identical to the 2D PCA (Fig. 4b). Hence, due to the similarities in 2D plots using PCA and ICA, it can be said the datasets were at their limit-reduced rank upon using PCA and characterized as independent sub-elements for the ICA technique.

Furthermore, interpreting the ICA 3D plot (Fig. 4e), it can be observed that all the five class clusters have

developed a similar elliptical nature as illustrated by PCA in Fig. 4c. Still, a significant dissimilarity is displayed when the fault severity increments. As the value of the fault increases, the corresponding elliptical plot elevates upwards as shown in the 3D ICA plot (Fig. 4e).

In addition to that, the 3D ICA plot captures not only the changes in the SITF severity, but also the varying load conditions. Unlike PCA, the fault severities are well separated together with the variation in the load (which is expressed in Fig. 4c).

## V. CLASSIFICATION USING NEURAL AND NON-NEURAL BASEDTechniques

Table II details a comparative analysis of the classification using the developed neural and non-neural based classifiers. It should be noted that LSTM architectures were developed using Python platform (packages: TensorFlow, Keras, Pandas, NumPy), while families of NN and Decision Tress are derived using MATLAB®.

TABLE II. COMPARATIVE ANALYSIS OF THE CLASSIFICATION MODELS (TEST ACCURACIES)

| Classifier | Class 1 Accuracy | Class 2 Accuracy | Class 3 Accuracy | Class 4 Accuracy | Class 5 Accuracy | Overall Accuracy | Comments |
|---|---|---|---|---|---|---|---|
| Unidirectional LSTM | 99.2 | 99.3 | 99.35 | 98.8 | 98.7 | **99.08** | 20% dropout rate, Architecture: $25_{IN}$ $\|16_{DL-tanh\ activation}\|1_{FL}\|5_{OUT-softmax\ activation}\|$, No. Parameters = 11321 |
| Deep LSTM | 99.45 | 99.3 | 99.2 | 98.6 | 98.6 | **99.04** | 20% dropout rate, Architecture: $25_{IN}$ $\|16_{DL-tanh\ activation}\|1_{FL}\|5_{OUT-softmax\ activation}\|$, No. Parameters = 43001 |
| Bidirectional LSTM | 99.15 | 99.05 | 98.65 | 98.5 | 98.5 | **98.77** | Architecture: $20_{IN}\|16_{DL-tanh\ activation}\|1_{FL}\|5_{OUT-softmax\ activation}\|$, No. Parameters = 12501 |
| Stacked LSTM | 99.2 | 98.8 | 98.85 | 98.6 | 98.65 | **98.82** | 10% dropout rate, Architecture: $20_{IN}\|16_{DL-tanh\ activation}\|20_{BL}\|5_{OUT-softmax\ activation}\|$, No. Parameters = 11157 |
| Bilayered NN | 98.5 | 95.3 | 86.3 | 82.3 | 89.3 | **90.3** | 2 FC: (20, 25), ReLU activation, 5 cross-fold validation, No. Parameters = 675 |
| Medium Tree | 77.5 | 85 | 93.3 | 85 | 91.3 | **86.4** | Max. splits: 600, Split Criterion: Gini's Diversity index, No. Parameters = 1057 |
| Wide NN | 75.7 | 63.5 | 45 | 71.5 | 81.8 | **67.5** | 1 FC: (100), 3 Layers: ReLU activation, 5 cross-fold validation, No. Parameters = 800 |
| Trilayered NN | 99.8 | 95.8 | 90 | 90.5 | 92.8 | **93.8** | 3 FC: (25, 20, 20), 3 Layers: ReLU activation, 5 cross-fold validation, No. Parameters = 1075 |
| Fine Tree | 77.5 | 93.3 | 85 | 85 | 91.3 | **86.4** | Max. splits: 500, Split Criterion: Gini's Diversity index, No. Parameters = 1057 |
| Narrow NN | 99.5 | 95.3 | 88.5 | 87.5 | 94.3 | **93.0** | 1 FC: (35), ReLU activation layer, 5 cross-fold validation, No. Parameters = 280 |

*DL filters in the dense layer
*FC neurons in a fully connected layer: (neurons)
*BL Bidirectional layer
*OUT neurons in the output layer
* IN input layer

Reviewing the classification performance of the neural based approaches, over 90% accuracy on the tests was achieved using family LSTM NNs and for other configurations of the neural-based models (Narrow, Tri-layered, and Bi-layered NN). On the other hand, the non-NN models consisting of the two modifications of Tree-based classifiers showed a reasonably good classification accuracy over 86%. With a few tweaks in constructing the tree models, such as; using different metrics to measure impurity (entropy) and using variations of maximum split values, the model accuracy can be enhanced. These non-linear-based techniques use a series of conditional statements to partition training data into subsets. Hence, each successive split adds more complexity to the model, which is used to make predictions [14].

The highest accuracies are undoubtedly seen for the four recurrent NNs (RNNs) architectures highlighted in gray. The bidirectional-LSTM model had been designed with an additional LSTM layer to allow the input sequence to flow forward and in the reverse direction of information using an additional layer. This architecture is designed as such, so the input sequence components can cater to the information from past and present states to produce more meaningful output. But for this application, the model accuracy falls a little short, with an accuracy of 98.77%.

The next model is the stacked LSTM, a similar configuration to Deep LSTM consisting of multiple hidden LSTM layers with an accuracy of 98.82%. The second highest classification accuracy was found within the deep LSTM with a test accuracy of 99.04% and 43,001 trainable parameters. Finally, the best performing architecture to

classify low severity SITFs considering the accuracy and least number of trainable parameters was the Unidirectional LSTM model with a test accuracy of 99.08% and 11,321 trainable parameters. The confusion matrix (classification trial's predicted class versus true class) and the receiver operating characteristic curve (ROC) for the best model (Unidirectional LSTM) is shown in Figs. 5 and 6, respectively.
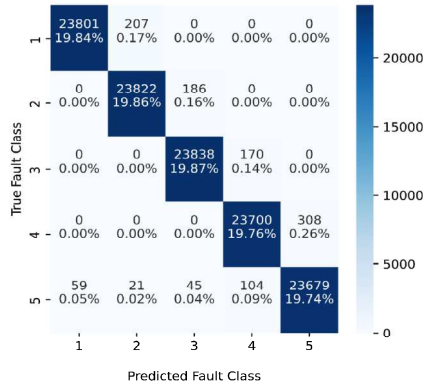


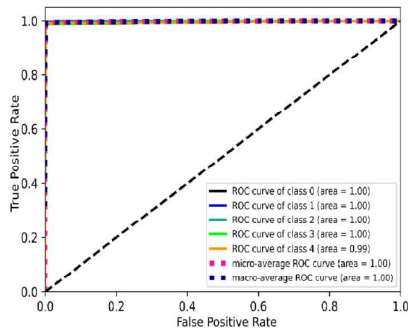Fig. 5. Confusion Matrix (Unidirectional LSTM)



Fig. 6. Receiver Operating Curve (Unidirectional LSTM)

## VI. CONCLUSION

In this paper, through the proposed approach, stator-interturn-faults with very low severities have been classified by suitably processing the 3-phase stator current signals. The analysis of geometry using PCA and ICA provides insight to understand and successfully distinguish the different class clusters (healthy and 4-fault classes) across various IM loading levels. This study shows the exploratory analysis and classification of the SITF at very low severities (0.3%-2.11%), which are not usually highlighted in other studies. Upon a thorough comparison of deep NN, shallow NN, and non-neural based models, the family of LSTM architectures achieve a test set accuracy greater than 98%. It is worth mentioning that the proposed strategy required no feature engineering step to classify the oncoming 3-phase signals. Amongst the LSTMs, the Unidirectional variant of LSTM NN proved to be the best classifier for SITFs at low severities, having least trainable parameters (11,321) out of the other LSTM variants and with the highest test accuracy of 99.08%.

Future works will build on the proposed strategy of classification and extend the idea on estimating the fault severities along with the fault classification.

## REFERENCES

[1] G. Mirzaeva and K. I. Saad, "Advanced Diagnosis of Stator Turn-to-Turn Faults and Static Eccentricity in Induction Motors Based on Internal Flux Measurement," IEEE Transactions on Industry Applications, vol. 54, no. 4, pp. 3961–3970, Jul. 2018, doi: 10.1109/TIA.2018.2821098.

[2] M. Hernandez-Vargas, E. Cabal-Yepez, and A. Garcia-Perez, "Real-time SVD-based detection of multiple combined faults in induction motors," Computers & Electrical Engineering, vol. 40, no. 7, pp. 2193–2203, Oct. 2014, doi: 10.1016/j.compeleceng.2013.12.020.

[3] G. H. Bazan, P. R. Scalassara, W. Endo, A. Goedtel, W. F. Godoy, and R. H. C. Palácios, "Stator fault analysis of three-phase induction motors using information measures and artificial neural networks," Electric Power Systems Research, vol. 143, pp. 347–356, Feb. 2017, doi: 10.1016/j.epsr.2016.09.031.

[4] M. Z. Ali, M. N. S. K. Shabbir, X. Liang, Y. Zhang, and T. Hu, "Machine Learning-Based Fault Diagnosis for Single- and Multi-Faults in Induction Motors Using Measured Stator Currents and Vibration Signals," IEEE Trans. on Ind. Applicat., vol. 55, no. 3, pp. 2378–2391, May 2019, doi: 10.1109/TIA.2019.2895797.

[5] S. Shao, R. Yan, Y. Lu, P. Wang, and R. X. Gao, "DCNN-Based Multi-Signal Induction Motor Fault Diagnosis," IEEE Trans. Instrum. Meas., vol. 69, no. 6, pp. 2658–2669, Jun. 2020, doi: 10.1109/TIM.2019.2925247.

[6] D. Xiao, Y. Huang, L. Zhao, C. Qin, H. Shi, and C. Liu, "Domain Adaptive Motor Fault Diagnosis Using Deep Transfer Learning," IEEE Access, vol. 7, pp. 80937–80949, 2019, doi: 10.1109/ACCESS.2019.2921480.

[7] D. Xiao, Y. Huang, L. Zhao, C. Qin, H. Shi, and C. Liu, "Domain Adaptive Motor Fault Diagnosis Using Deep Transfer Learning," IEEE Access, vol. 7, pp. 80937–80949, 2019, doi: 10.1109/ACCESS.2019.2921480.

[8] L. A. Garcia-Escudero, O. Duque-Perez, M. Fernandez-Temprano, and D. Morinigo-Sotelo, "Robust Detection of Incipient Faults in VSI-Fed Induction Motors Using Quality Control Charts," IEEE Trans. on Ind. Applicat., vol. 53, no. 3, pp. 3076–3085, May 2017, doi: 10.1109/TIA.2016.2617300.

[9] K. K. Raj, S. H. Joshi, and R. Kumar, "A state-space model for induction machine stator inter-turn fault and its evaluation at low severities by PCA," in 2021 IEEE Asia-Pacific Conference on Computer Science and Data Engineering (CSDE), Dec. 2021, pp. 1–6. doi: 10.1109/CSDE53843.2021.9718479.

[10] R. R. Kumar, G. Cirrincione, M. Cirrincione, A. Tortella, and M. Andriollo, "Induction Machine Fault Diagnosis Using Stator Current Subspace Spectral Estimation," in 2018 21st International Conference on Electrical Machines and Systems (ICEMS), Jeju, Oct. 2018, pp. 2565–2570. doi: 10.23919/ICEMS.2018.8549374.

[11] R. R. Kumar, G. Cirrincione, M. Cirrincione, A. Tortella, and M. Andriollo, "A Topological Neural-Based Scheme for Classification of Faults in Induction Machines," IEEE Trans. on Ind. Applicat., vol. 57, no. 1, pp. 272–283, Jan. 2021, doi: 10.1109/TIA.2020.3032944.

[12] B. Saddam, B. S. Ahmed, A. Aissa, and T. Ali, "Squirrel Cage Induction Motor under Stator and Rotor Bars Faults Modeling and Diagnosis," in 2018 International Conference on Communications and Electrical Engineering (ICCEE), El Oued, Algeria, Dec. 2018, pp. 1–6. doi: 10.1109/CCEE.2018.8634502.

[13] S. Bachir, S. Tnani, J.-C. Trigeassou, and G. Champenois, "Diagnosis by parameter estimation of stator and rotor faults occurring in induction machines," IEEE Trans. Ind. Electron., vol. 53, no. 3, pp. 963–973, Jun. 2006, doi: 10.1109/TIE.2006.874258.

[14] B. Jijo and A. Mohsin Abdulazeez, "Classification Based on Decision Tree Algorithm for Machine Learning," Journal of Applied Science and Technology Trends, vol. 2, pp. 20–28, Jan. 2021.